Int J Fract (2013) 180:23–39
DOI 10.1007/s10704-012-9793-0

ORIGINAL PAPER

Ductile failure behavior of polycrystalline Al 6061-T6 under shear dominant loading

A. Ghahremaninezhad · K. Ravi-Chandar

Received: 29 May 2012 / Accepted: 16 November 2012 / Published online: 4 January 2013

Abstract Ductile failure in polycrystalline aluminum alloys under pure shear as well as with superposed tension and compression loading is explored through the modified Arcan shear experiments. Specimens obtained through tests interrupted at various stages of deformation and failure evolution are examined through quantitative microscopy to discern the mechanisms of failure and to evaluate the local strain evolution quantitatively. Fractographic observations are used to identify the onset and evolution of damage processes during deformation and failure of these aluminum alloys. Local strain levels are estimated from measurements of the change in grain size with deformation and used to indicate that the local values of failure strains are likely to be much larger than that estimated from strains averaged over characteristic specimen dimensions such as the gage length or the specimen diameter. Lower bound estimates of the failure strain in low triaxiality conditions are obtained from the experiments. It is shown that strain-to-failure decreases monotonically with stress triaxiality in stark contrast with recent works where a reverse behavior in low stress triaxiality levels was reported. Eventual failure that occurs through void growth and coalescence is shown to be restricted to a very small region within the localized deformation band.

Keywords Arcan specimen · Damage nucleation · Failure mechanism · Local strain measures · Strain-to-failure

A. Ghahremaninezhad · K. Ravi-Chandar (✉)
Center for Mechanics of Solids, Structures and Materials, The University of Texas at Austin, Austin, TX, 78712-0235, USA
e-mail: ravi@utexas.edu

Present Address:
A. Ghahremaninezhad
Department of Civil, Architectural, and Environmental Engineering, University of Miami, Coral Gables, FL 33124, USA

1 Introduction

Most models for ductile failure based on void growth and coalescence—such as the Gurson–Tvergaard–Needleman (GTN) model—indicate that there is no accumulation of damage under pure shear deformation where the triaxiality is zero; therefore, no localization or failure could be predicted under these loading conditions. There have been recent attempts to trigger failure under shear through ad hoc modifications of the GTN, but without incorporating micromechanical mechanisms of damage. It should be noted that in many engineering applications, the onset of strain localization is taken to be the point of failure—for example, the forming limit diagram is of interest in sheet metal forming. However, this does not constitute material failure and therefore the strain level measured at the onset of strain localization cannot be used as a measure of "strain-to-failure"—meaning material separation and generation of new surfaces—and used in quantitative predictions of ductile failure. In this paper, we address

the issue of how failure occurs under pure shear and combined shear plus normal loading conditions, with particular attention to the Al 6061-T6 sheet[1] material used by Ghahremaninezhad and Ravi-Chandar (2012) and to examine the local strain state prior to such failure. Future studies will focus on examining and modeling the actual fracture process.

Numerous investigators have examined the problem of failure under shear dominant loading through different experiments. For example, Rogers (1960) examined ductile failure in OFHC copper with a (fairly large) grain size of about 1 mm; after examination of metallographic sections from uniaxial tests interrupted at various stages of neck growth, Rogers concluded that in the cup and cone type of fracture, subsequent to the growth of the central crack, failure occurred by concentration of shear at an angle of 30°–40° to the tensile axis through the nucleation of a large number of voids within this shear zone and their eventual coalescence; this is called the "void sheet mechanism". Puttick (1960) also explored the basic deformation and failure mechanisms in polycrystalline copper. The material had a grain size of about 50 μm, and contained impurities that were introduced during the solidification process. These specimens developed standard cup-and-cone fractures that began with the formation of a diffuse necking localization. The formation of a macroscopic shear band and void coalescence within the shear band were also identified by Puttick (1960). These careful metallographic observations clearly revealed that the mechanism of failure under shear in ductile materials is the nucleation and growth of cavities but localized within the shear band. It should, however, be noted that these failures were observed in specimens with a triaxiality—ratio of the equivalent stress to the mean stress—in the range of 0.67–1. For pure shear type loading, Lindholm et al. (1980) developed a torsion apparatus for subjecting specimens to large strain levels at various strain rates; they examined the shear response of thin-walled tubes of annealed OFHC copper in the strain rate range of 0.009 s^{-1} to about 330 s^{-1}. The grain size in the specimen ranged from about 25–35 μm. Specimens strained at rates below 10 s^{-1} exhibited positive strain and strain-rate hardening; more importantly, *no localization of deformation was observed even at a true (logarithmic) strain level of about two*. At strain rates greater than 174 s^{-1}, localized shear deformation was observed at a strain level of about 1.6; failure under shear was not attained even in these tests. This inability to trigger failure under pure shear in a torsion test is rather well-known; however, in recent years, Bao and Wierzbicki (2004), Beese et al. (2010) and others have investigated failure under low triaxiality conditions using a butterfly shaped specimen, where both the triaxiality and the Lode angle—a measure of stress-state related to the third invariant of the deviatoric stress tensor—can be controlled by selecting the combination of tangential and normal loading at the specimen boundaries. Barsoum and Faleskog (2007) also examined failure in a Weldox steel under low triaxiality conditions by performing combined tension-torsion experiments in specially-designed doubly-notched tubular specimens. In many of these experiments, the reported strain-to-failure under low triaxiality conditions is lower than the strain-to-failure at higher triaxiality conditions. An example of such a trend, obtained by Beese et al. (2010) for Al 6061-T6, is shown in Fig. 1. The main difference between these results and the earlier experiments of Hancock and Mackenzie (1976) and Johnson and Cook (1985) is in the region of low triaxiality; while the earlier results reported a monotonic increase in the strain-to-fracture with decreasing triaxiality, the results of Beese et al. (2010) and Barsoum and Faleskog (2007) indicate a nonmonotonic dependence, with a cusp at different triaxiality levels for different materials and a drop in the strain-to-failure at lower triaxialities. While results of this type have led to the development of void growth models that incorporate shear effects in a phenomenological manner (see Nahshon and Hutchinson 2008), it is important to understand the experimental procedure used to identify such strain-to-failure. The strain-to-failure reported in these works is typically obtained using a hybrid procedure: an experiment is performed under pure shear or a shear plus a normal load under combined torsion and tension or compression. The force–elongation response of the specimen is monitored to identify the onset of failure; Beese et al. (2010) use the surface strain in the gauge section, measured using the digital image correlation (DIC) technique, as the strain-to-failure, while Barsoum and Faleskog (2007) use a numerical simulation of the experiment to calculate the strain at the midpoint in the specimen and use this value as the strain-to-failure. As demonstrated by Ghahremaninezhad and

[1] Results of a study on ductile failure under combined tension and torsion in tubular specimens is reported in another recent contribution (Haltom et al. 2012).

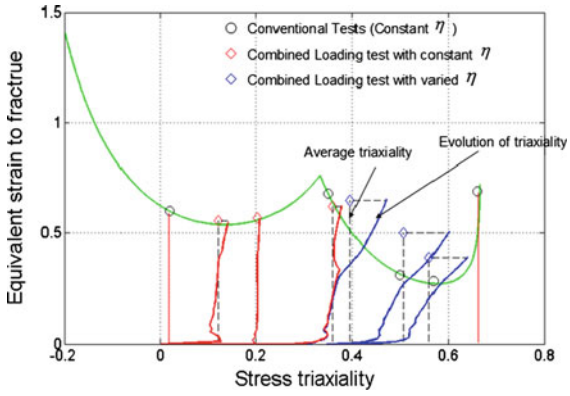

Fig. 1 Modified Mohr-Coulomb fracture criterion proposed by Beese et al. (2010) for Al 6061-T6; note the cusp in the failure strain for triaxialities around 0.3 (reproduced with permission)

Ravi-Chandar (2011, 2012), these procedures are not quite suitable for determination of the local strains at failure; characterization of failure requires careful identification of the exact location of failure initiation and a proper definition of a gage length over which such strains are measured. In addition, under complex loading conditions, failure is seldom within the gauge section of the specimen where observations and measurements are typically performed, but at locations of stress concentration that are unavoidable in these geometries. Therefore, it is imperative that the details of strain evolution in the specimen be examined carefully. In this paper, we explore failure under shear loading through local measurements obtained at the grain level.

There is a large body of literature that deals with mixed-mode fracture in specimen configurations that are dominated by the stress concentration associated with a single dominant crack. For example, Aoki et al. (1990), explored ductile failure under mixed mode loading in steels and aluminum alloys; and showed that shear band formation was dominant in triggering failure. Ghosal and Narasimhan (1994, 1996, 1997) performed finite element studies of crack response under mixed mode loading using a Gurson model, and examined various aspects of the problem, such as the debonding of inclusions, the deformation and sharpening of the notch, and the dependence of the fracture toughness on the mode mixity. An interesting study by Roy et al. (1999) examined the notch tip response and provided some micrographic evidence of cavity nucleation near the notch tip. The goal of the studies cited above and others (such as Kamat and Hirth 1996) was mainly to investigate the dependence of the fracture toughness, characterized in terms of the J-integral, on mode-mixity. In contract, the present paper is concerned with examination of the evolution of deformation and the initiation of failure in specimens without an initial crack; of course, these results will eventually be applied to simulations of cracked geometries with the understanding that the mechanisms of deformation and failure must exhibit similarity in the two problems.

This article is organized as follows: the experimental scheme and measurements for pure shear loading and shear loading with superposed compression or tension is described in Sect. 2. This is followed in Sect. 3 by a microscopic examination of the evolution of deformation at the grain level, and a scanning electron microscopic investigation of the onset and progression of damage. The measurements and observations are discussed in Sect. 4, with the aid of numerical simulations of the stress-state. The main conclusions are summarized in Sect. 5.

2 Experiments

We perform experiments in a modified Arcan type specimen; DIC-based macroscopic strain measurements,[2] grain-based microscopic strain measurements, and optical and scanning electron microscopy are used to monitor the strain at multiple length scales, to identify the onset of failure, and to explore the mechanisms of deformation and failure under shear dominant loading conditions. The Arcan specimen has been used in numerous studies of composite materials (see for example, Hung and Liechti 1997, 1999). There have also been some investigations aimed at characterizing the effects of the notch angle on the shear response of the specimen (Hung and Liechti 1997, 1999); in the present work we used a 45° notch angle. A modified version of the Arcan configuration has been used by Dunand and Mohr (2011) to examine failure in a dual phase steel. The loading in this test is applied in a fully clamped configuration through a dual actuator system and the stress state is controlled not only by the 2D

[2] The commercial software ARAMIS^{TM}, supplied by GOM, Germany was used to perform the DIC measurements. The displacements were interpreted in terms of the true (logarithmic) strains based on gage lengths that were in the range of about 165 μm.

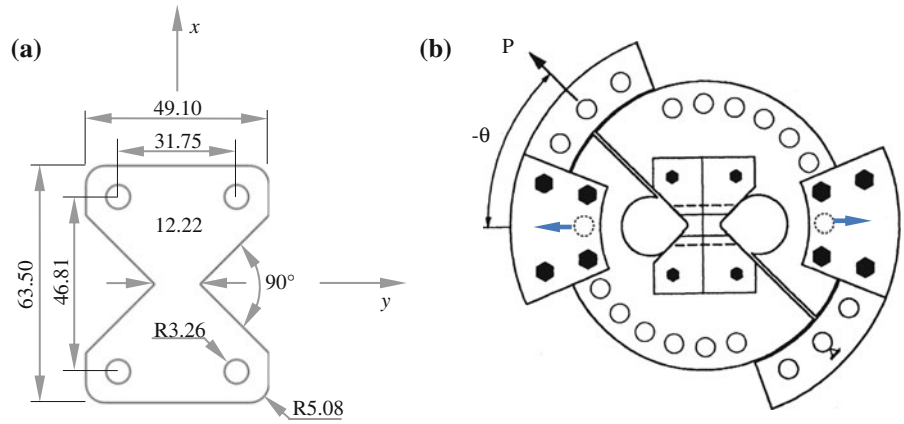

Fig. 2 **a** Geometry of the Arcan specimen (all dimensions are in mm). Rolling direction is along the x-direction. **b** Geometry of the fixture used in the modified Arcan tests (reproduced from Hung and Liechti 1999). The *two arrows* from the *dotted circles* indicate pure shear loading; other pairs of holes result in shear plus compression or tension

shape of the specimen, but also through a local reduction of the gage section thickness that was estimated through numerical analysis; these modifications generate failure at a predictable location within the gage section of this specimen. The geometry of the Arcan specimen used in the present work is shown in Fig. 2a; specimens were cut from the same rolled sheet stock (2.44 mm thick) used for the tension tests described in Ghahremaninezhad and Ravi-Chandar (2012), with the rolling direction oriented along the x-direction as indicated in Fig. 2a. These specimens were loaded in a modified Arcan fixture shown in Fig. 2b. Both pure shear loading and shear with superposed normal tensile or compressive loads were considered. It is true that the Arcan specimen introduces strain concentration and therefore failure initiation at the edges; however, we do not see this as a problem since we do not interpret the results based on homogeneity of the specimen, but infer local strains through careful *local* measurements. Also, buckling may occur in the Arcan experiment depending on the thickness of the specimen. Initial parametric studies with different geometries were performed and the final specimen geometry was chosen such that shear buckling was not observed in the numerical analysis. Also, we did not observe shear buckling in the experiment. The results from these experiments are discussed in the following subsections.

2.1 Pure shear

The nominal stress (force/initial gage cross-sectional area) versus normalized crosshead displacement response curves from three pure shear tests are shown

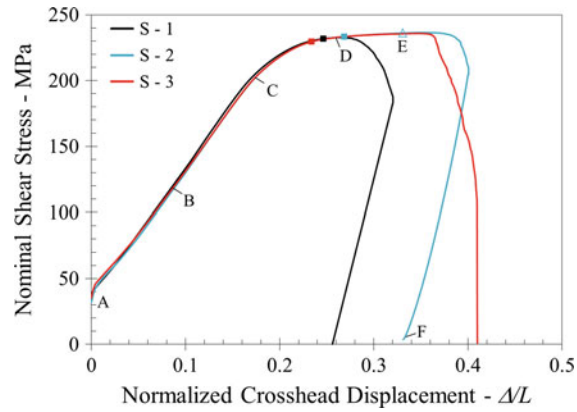

Fig. 3 Nominal shear stress (force/initial gage cross-sectional area) versus crosshead displacement (Δ) normalized by the gage length ($L = 12.22$ mm; see Fig. 2a) response of Specimens S-1, S-2 and S-3. *Square* symbols mark the initiation of the crack at the notch tips for the three specimens and the *triangle* symbol marks the last image of Specimen S-2 where DIC was able to provide local strain measurements

in Fig. 3; these specimens (S-1, S-2, S-3) were fabricated by electric discharge machining (EDM), resulting in a radius of curvature at the notch tip of 160 μm. One specimen was loaded to complete failure and the other two were unloaded after crack initiation from the notch area and partial crack growth across the specimen. Note that all specimens were preloaded in order to remove any slack in the loading fixture. The development of strain in all these tests was monitored using DIC (with the untested specimen serving as the reference image); for the specific implementation of DIC used in this work, the displacements are measured at nodes with a spacing of 82.5 μm and strains are determined with a gage length of 165 μm; the displacement resolution

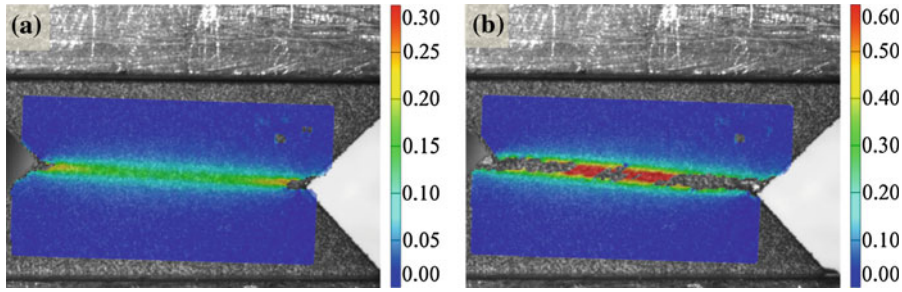

Fig. 4 Contour plots of the maximum principal strain **a** corresponding to crack initiation at the notch tips and **b** at the last stage where digital image correlation still provides an evaluation of strains (Specimen S-2)

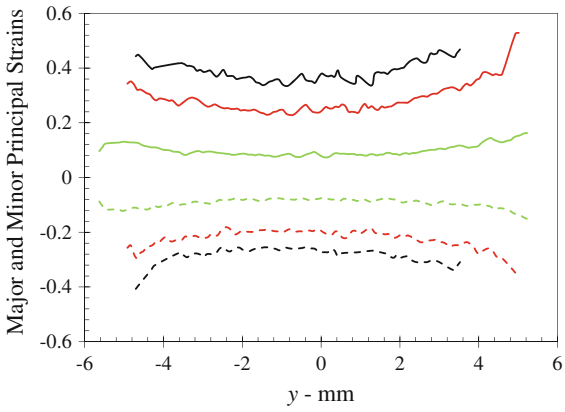

Fig. 5 Variation of the maximum (*solid lines*) and minimum (*dashed lines*) principal strains between the two notches at normalized crosshead displacements $\Delta/L = 0.199$ (*green*), 0.255 (*red*) and 0.272 (*black*)

is $\sim 10\,\mu$m. From these gage lengths, it should be evident that the strains near the notch tip region could not be resolved. The labels A through F in Fig. 3 indicate loading conditions at which the deformation of the centerline ($-1 < x < 1; y = 0$) of Specimen S-2 will be discussed in greater detail. The maximum principal strain contours at two selected stages, one corresponding to the onset of crack growth and the other corresponding to the last loading stage where image correlation is able to provide measurements of local strain for Specimen S-2 are shown in Fig. 4. Note that the material continues to strain beyond this point; however, local strain measures are not accessible through DIC as a result of speckle degradation, image decorrelation and other unavoidable limitations of the DIC. The variation of the maximum and minimum principal strains between the two notches at selected stages in the loading history is shown in Fig. 5. From these experiments, we record the following observations:

a. The nominal shear stress vs. normalized crosshead displacement response of all specimens follows a similar trend until crack initiation (see Fig. 3). The point of crack initiation, identified visually from the digital images, is marked in the figure; there is a small variability in the load at the onset of crack growth, attributable to errors in visual identification of crack initiation, and to statistical variability in the material and specimens.

b. It can be seen from Fig. 4 that the overall deformation is concentrated between the two notches. Quantitative variation shown in Fig. 5 suggests that maximum and minimum principal strains along the line ($x = 0$) are nearly uniform over the mid-region of the specimen in the early stages of loading, but become significantly non-uniform with increasing global strain; in particular the notch tip regions experience significantly enhanced tensile and compressive strains; the largest strains occur near the notch, but these are not resolved accurately by the DIC technique. It is, of course, to be expected that cracks would nucleate and grow from the two notches; indeed, this is what is observed, before the peak load is reached; nucleation of the crack was identified visually from the speckled images. With further global loading, these cracks grow across the width towards each other until they meet near the center of the specimen leading to the final separation. The details of crack initiation are not resolved in the images obtained for the DIC measurements; this requires real-time microscopic examination that was not performed in the present work and will be addressed in a future contribution.

c. Comparing the maximum and minimum principal strain variation shown in Fig. 5, and using plastic incompressibility, it is easy to see that the strain

in the thickness direction of the specimen must be nearly zero; therefore, it can be assumed that only in-plane strains are present in the specimen until significantly large strain levels approaching failure are attained. This observation should be restricted to the regions away from the notch since this is where the DIC strain measurements are reliable.

d. Strain measurements obtained with DIC could not resolve the strains in the vicinity of the crack tips at the onset of final failure due to the highly localized deformation in the vicinity of the propagating cracks. Even in the central portion of the specimen, as the true principal strain levels reach about 0.6, the speckle patterns become decorrelated and larger strain levels could not be measured. The strain contour corresponding to the last analyzed image for Specimen S-2 is shown in Fig. 4b; the corresponding points are marked on the nominal shear stress vs. normalized crosshead displacement response in Fig. 3. It is seen that maximum principal strain levels at the central region of the gage section are in the range of 0.6. These strains are similar to the values reported by Beese et al. (2010) as the failure strain for pure shear, but it should be emphasized that in our measurements these are not estimates of the strain at which the material fails; these are merely the strains at the center of the specimen, when failure occurs in the specimen. Actual failure of the material initiates from the strain concentration at the notch tips which then generates a crack at both notches; failure in the central locations occurs as these cracks propagate gradually towards the center. We will investigate the strains in these regions further in Sect. 3 through optical and scanning electron microscopy.

e. The deformed shape of a 2 mm long segment of the centerline ($-1 < x < 1; y = 0$) of Specimen S-2, as determined from DIC, is shown in Fig. 6 at different stages (marked as A through F in Fig. 3) in the overall loading of the specimen; from these lines, it is easy to visualize the deformation of this line segment. However, image correlation is lost in the regions of large strains as a result of changes in the surface texture, reflectivity of the specimen or due to the paint peeling off (see Fig. 4b). Even though the maximum strain levels *measured* using DIC are only about 0.6, it is clear that these are not the maximum strain levels sustained by the material prior to failure; the central portion of the specimen continues to strain even after the DIC method fails to provide estimates of the strain. A simple extrapolation, based on connecting the displacements of points correlated by DIC, yields shear strain levels of 0.83; we will extract the actual strains in this region by using grain-based strain measurements and compare the DIC based deformation with grain based measurements in the next section.

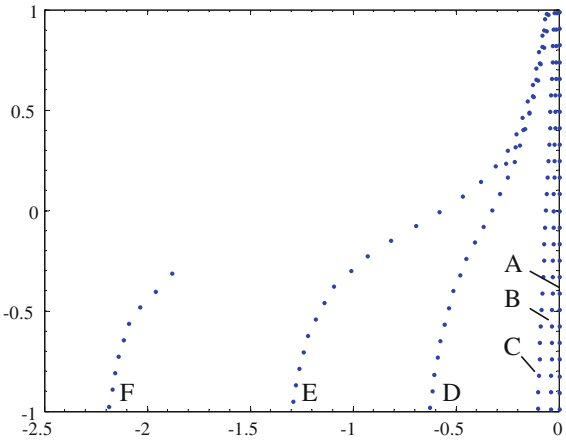

Fig. 6 The deformed shape of a 2 mm long segment of the centerline ($-1 < x < 1;\ y = 0$) of the specimen S-2, as determined from DIC at different stages A–F in the overall loading of the specimen as marked in Fig. 3

2.2 Shear with superposed normal loading

Ten additional tests were performed; in these tests, the specimens were loaded in the Arcan fixture shown in Fig. 2b at six different angles ($-15°$, $0°$, $15°$, $30°$, $45°$ and $60°$) giving rise to six different loading combinations—pure shear (specimens S-4 and S-5), shear plus tension (specimens ST-15, ST-30, ST-45 and ST-60) and shear plus compression (SC-15), respectively. Specimens S-4, S-5, ST-15 and SC-15 were mill-cut and therefore the notch tip radius was 800 μm; two specimens of each ST-30, ST-45 and ST-60 were made using EDM as described before, with one loaded all the way to the failure and the other unloaded prior to final failure. The nominal stress vs. normalized crosshead displacement response curves from these tests in six different loading orientations are shown in Fig. 7.

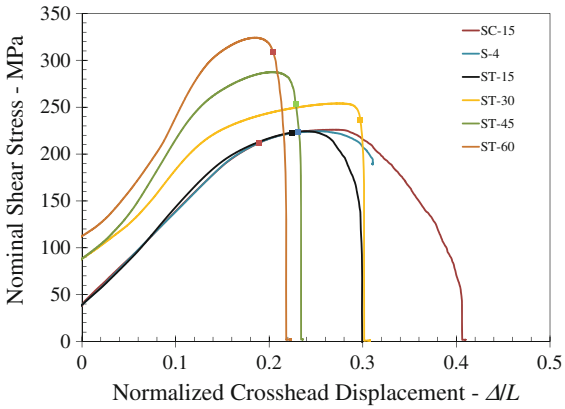

Fig. 7 Nominal shear stress (force/initial gage cross-sectional area) versus crosshead displacement (Δ) normalized by the gage length ($L = 12.22$ mm; see Fig. 2) response of Specimens SC-15, S-4, ST-15, ST-30, ST-45 and ST-60. *Square* symbols mark the initiation of the crack at the notch tips for each specimen

The maximum principal strain contours corresponding to the last loading stage where image correlation is able to provide measurements of local strain for Specimens SC-15, S-4 and ST-15 are shown in Fig. 8. As with the pure shear specimens, these specimens continue to strain beyond the point where DIC fails; therefore; local stain measures are not available beyond this point from DIC. The response of these specimens appear to be very similar to that observed under pure shear. In particular, the maximum and minimum principal strains along the specimen center are in the same range as the pure shear specimens. In all these tests, the maximum strains recorded by DIC are in the range of 0.6, but as noted before this does not correspond to failure of the material. Contour plots of maximum principal strain of Specimens ST-30, ST-45 and ST-60 corresponding to the last image at the onset of failure are shown in Fig. 8; the maximum principal strain in the central region of these specimens are in the range of 0.30, 0.24 and 0.18, respectively. It is noted that these values are much smaller than that in the case of pure shear, and unlike in the latter case where the image decorrelation inhibited the calculation of the strains by DIC in the central portion of the gage section, in the former cases DIC could correlate the strain in this region up to the onset of specimen failure. However, as will be shown in the next section through grain level measurements of the strain in these specimens, *the strains measured using DIC are not the failure strain in the material*.

3 Microscopic examination of deformation and damage

In an effort to determine the local strains and identify the onset of damage, a number of specimens were cut to reveal the microstructure in the x–y plane, mounted in epoxy, polished, and etched using Weck's etchant (details of the specimen preparation for metallographic observations are given in Ghahremaninezhad and Ravi-Chandar 2012). In order to examine the evolution of deformation at the grain level, optical micrographs of the prepared sections were taken and stitched together to explore a large spatial domain. Damage evolution in the same specimens was investigated through scanning electron microscopy.

3.1 Optical microscopy and grain-based strain measurements

Optical micrographs of the regions near the left notch and at the center of the Specimen S-2 (loaded in pure shear) are shown in Figs. 9a and 10a, respectively. The deformation at the grain level can be identified clearly by comparing these images with the undeformed grain structure in the x–y plane in Fig. 1a of Ghahremaninezhad and Ravi-Chandar (2012). High-magnification images of the rectangular regions marked as 'I', 'II' and 'III' in these optical micrographs are also shown in Figs. 9b, c and 10b, respectively. At locations far away from the line connecting the two notches (region I), the grains remain nearly undeformed; these grains shown in Fig. 9b can be compared to the initial grain distribution in the $x - y$ plane shown in Fig. 1a of Ghahremaninezhad and Ravi-Chandar (2012). As indicated there, the undeformed grains in the x–y plane are nearly equiaxed, with an average grain size of about 46 μm in the x-direction and 39 μm in the y-direction. Large deformation and rotation of the grains can be readily identified from the micrographs in Figs. 9c and 10b, with these images corresponding to regions II and III near the notch and the center of the specimen, respectively. The images in Figs. 9 and 10 indicate that these large deformations are confined to a very narrow region in the specimen. We now turn to quantitative estimates of the deformation. The grain width changes are measured and interpreted in terms of the equivalent plastic strain at the grain level using the procedures indicated in Ghahremaninezhad and Ravi-Chandar

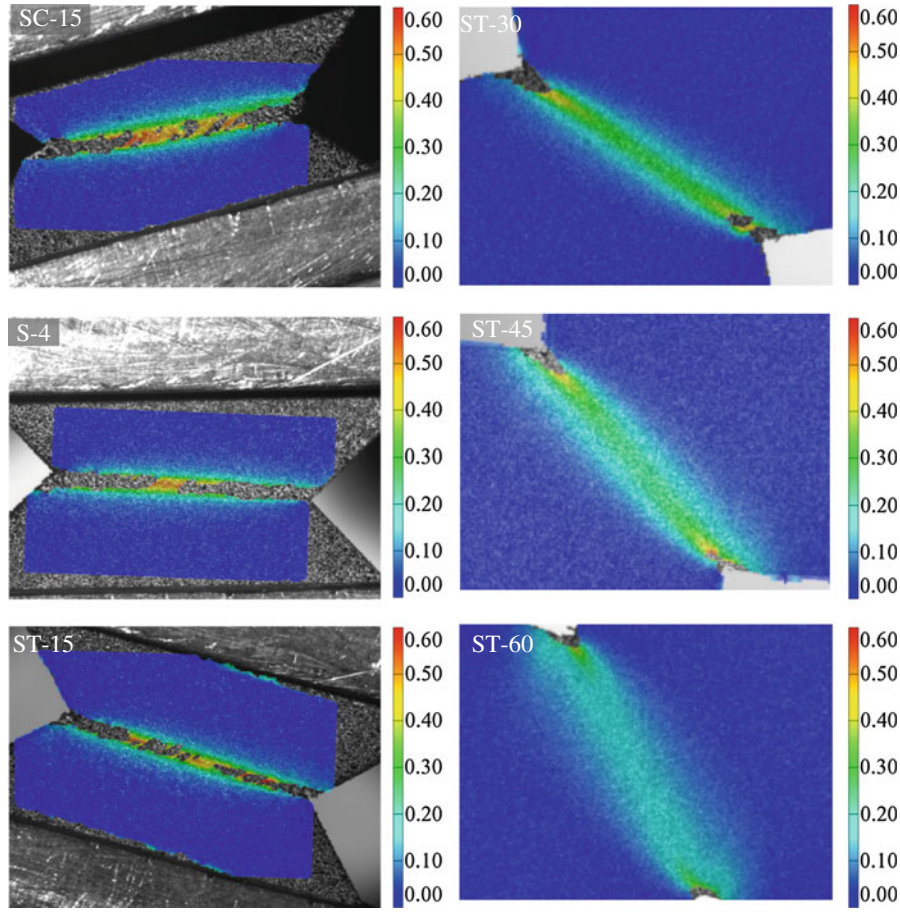

Fig. 8 Contour plots of the maximum principal strain in Specimens SC-15, S-4, ST-15, ST-30, ST-45 and ST-60. Loading corresponds to the last stage where DIC was able to correlate the images for SC-15, S-4 and ST-15, and to the last image at onset of fracture for ST-30, ST-45 and ST-60

(2012): first, the average, $\hat{w}$, and standard deviation, $\Delta\hat{w}$, of the minor axis of equivalent ellipses of the grains were estimated from the images of the initial microstructure. Next, the variation of the minor axis w of the equivalent ellipses of the deformed grains across the dashed lines in Fig. 9 was obtained, and divided by the mean initial grain size to obtain an estimate of the minimum principal strain $\varepsilon_{\min} = \ln\left(w/\hat{w}\right)$. Based on the DIC measurements, we are assured that a condition of in-plane deformation is satisfied in the regions away from the notches, and hence the maximum principal strain is $\varepsilon_{\max} = -\varepsilon_{\min}$ and the equivalent plastic strain can be estimated to be $\varepsilon_{eq} = \left(2/\sqrt{3}\right)\ln\left(\hat{w}/w\right)$. In order to decrease the scatter in the data, the deformed grain thickness was averaged over five neighboring grains (along the y-direction), two on either side. The variation of the grain level strain across five lines, marked as Lines 1–5 on the micrographs of Specimen S-2 in Figs. 9a and 10a is shown in Fig. 11. These grain-based measurements reveal that the Al 6061-T6 experiences significant strains prior to failure. The grain level measurements reveal a number of features of the deformation:

a. It is possible to reconcile the grain based measurements with the image correlation based measurements. Recall that the deformed shape of the line $(-1 < x < 1; y = 0)$ was plotted at different stages of the macroscopic loading in Fig. 6; the last of these lines (Stage F) corresponds to the final stage of loading. While digital image correlation was not able to provide the displacements in the central region, displacements outside this region were indeed measured. The grain flow lines can be identified from Fig. 9c and correlated with the far field DIC measurements.
b. Line 5 corresponds to the centerline of the specimen $(-1 < x < 1; y = 0)$, when the crack has not yet propagated through this region. It is clear from Fig. 10a that very high strains, in the range of about 1.5–2 appear over a band of about 500 μm

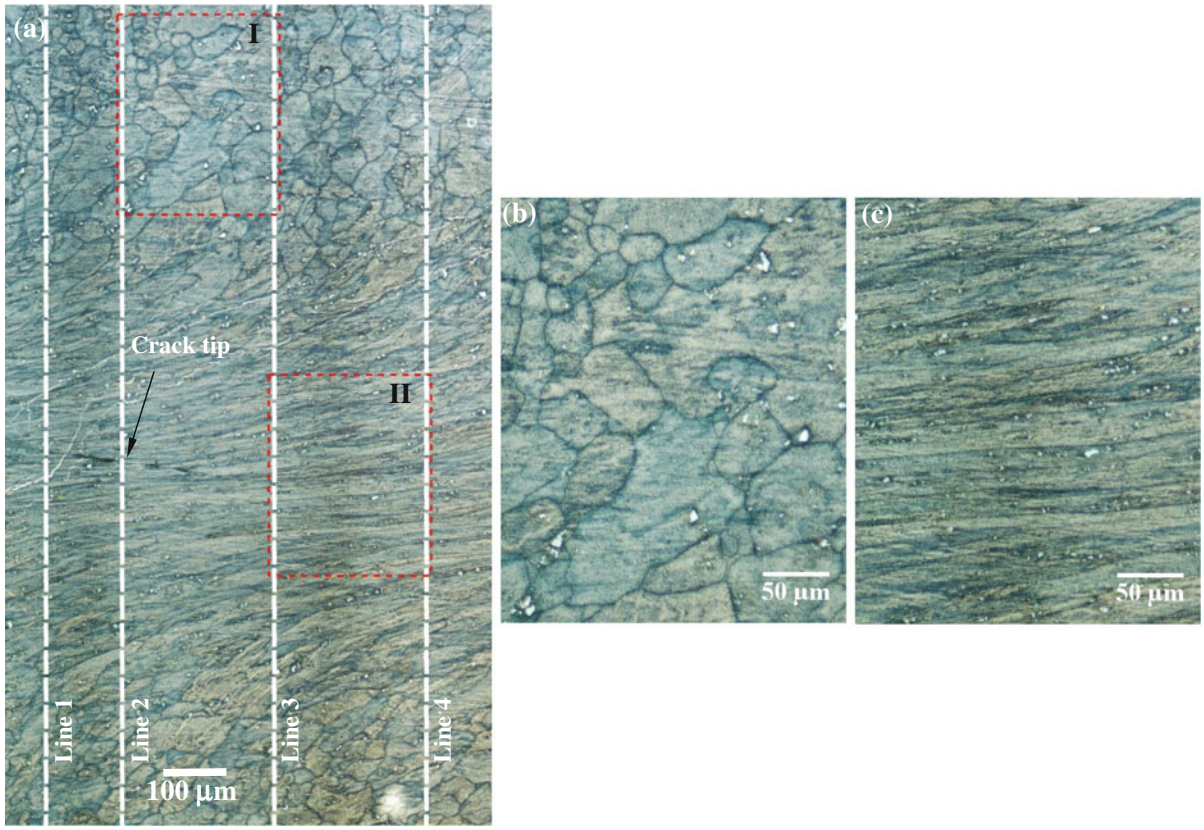

Fig. 9 **a** Optical micrograph of the region near the notch of Specimen S-2. **b** High magnification view of region I, away from the highly deformed area. **c** High magnification of region II in the highly deformed area

thickness in the central part of the specimen. These strain levels are significantly larger than the largest strains measured by digital image correlation because they arise after the point where the DIC technique fails to correlate. Outside of this band, the strains decrease sharply.

c. The highest strain levels near the crack surface and crack tip (along Lines 1–4) are in the range of 2. The grains can be seen to have rotated by nearly 90° near the notch tips and appear to be aligned along the horizontal direction as can be seen in Fig. 9c. In the interior parts, the rotation is greater than about 70°. The size of the band over which the strain is localized in the vicinity of the crack is smaller ($\sim 400\,\mu$m) than that of the band in the central portion of the specimen.

Specimens SC-15 and ST-15 were both loaded to complete failure; the micrographs of these specimens resemble closely the deformation of Specimen S-2. Micrographs of approximately half the gage section of Specimen ST-30 is shown in Fig. 12a. The regions in the center and near the notch of Specimens ST-45 and ST-60 are shown in Fig. 12b, respectively. The following observations are reported:

a. Comparing the grain width and orientation in these micrographs with those in the pure shear tests, it is easy to recognize that rotations and deformations generated near the middle of the specimens are somewhat smaller than in the case of pure shear.
b. Similar to pure shear loading, cracks initiated near both notch tips, and propagated towards the center portion of the gage section (Fig. 12b). Grains near the crack surface can be seen to have rotated and deformed much more than in the middle region, under combined shear and tension.
c. Unlike the case of the pure shear tests, the strain in the thickness direction was not negligible; however, the equivalent plastic strain was esti-

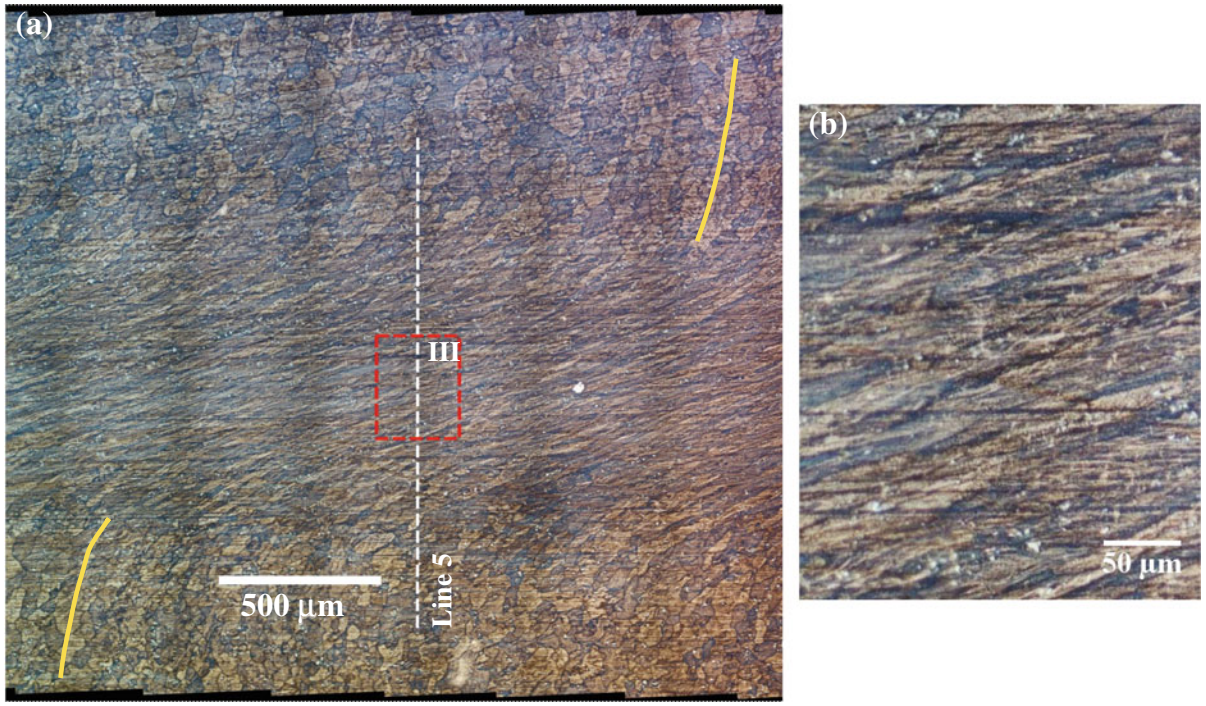

Fig. 10 **a** Optical micrograph of the region near the middle of Specimen S-2. The *yellow line* corresponds to the deformation of Line-5 as measured by DIC at stage F. **b** High magnification view of the highly deformed area (region III)

mated initially using the same procedure discussed above for the pure shear tests: $\varepsilon_{eq} = \left(2/\sqrt{3}\right) \ln\left(\hat{w}/\hat{w}_{2\times5}\right)$ where $\hat{w}$ is the average undeformed grain size, and $\hat{w}_{2\times5}$ is the *equivalent ellipse minor axis* averaged over an area containing 2×5 grains in x-and y-directions, respectively. Variation of the equivalent strain in Specimen ST-30 along the Line-1 and Line-3, limited between two yellow lines in Fig. 12a is shown in Fig. 12c. Strain values in the range of about 1–1.3 exist in the region near the crack tip and decrease with distance from the crack tip.

These microscopic observations and measurements based on grains indicates that very large strain levels are attained in the Al 6016-T6 specimens prior to failure under shear loading. However, while the optical micrographs are able to provide quantitative estimates of the local strains at the level of the grains, the onset of damage, particularly at the micron to sub-micron level is not readily observed even though the second phase particles are visible in the optical micrographs; for this purpose, we turn to scanning electron microscopy.

3.2 Evaluation of damage using scanning electron microscopy

In order to explore the onset of failure, optical and scanning electron micrographs of Specimen S-5, which was completely broken under pure shear, were obtained. Figure 13a shows an optical micrograph of the central region of this broken specimen; Fig. 13b shows a scanning electron micrograph of the same region. A composite image is made by overlaying the SEM image onto the corresponding optical image with opacity of 0.6 (see Fig. 13c); this enables identification of the relationship between the location of the grain boundaries and the second phase particles. The following features can be observed:

a. While the second phase particles are distributed randomly in the initial microstructure, (see Fig. 17 in Ghahremaninezhad and Ravi-Chandar 2012), these particles appear to have been reoriented, aligned and more or less collected together in clusters by the deformation! It is noted that the mean size of the second phase particles in the initial microstructure is about 2 μm wide and 10 μm

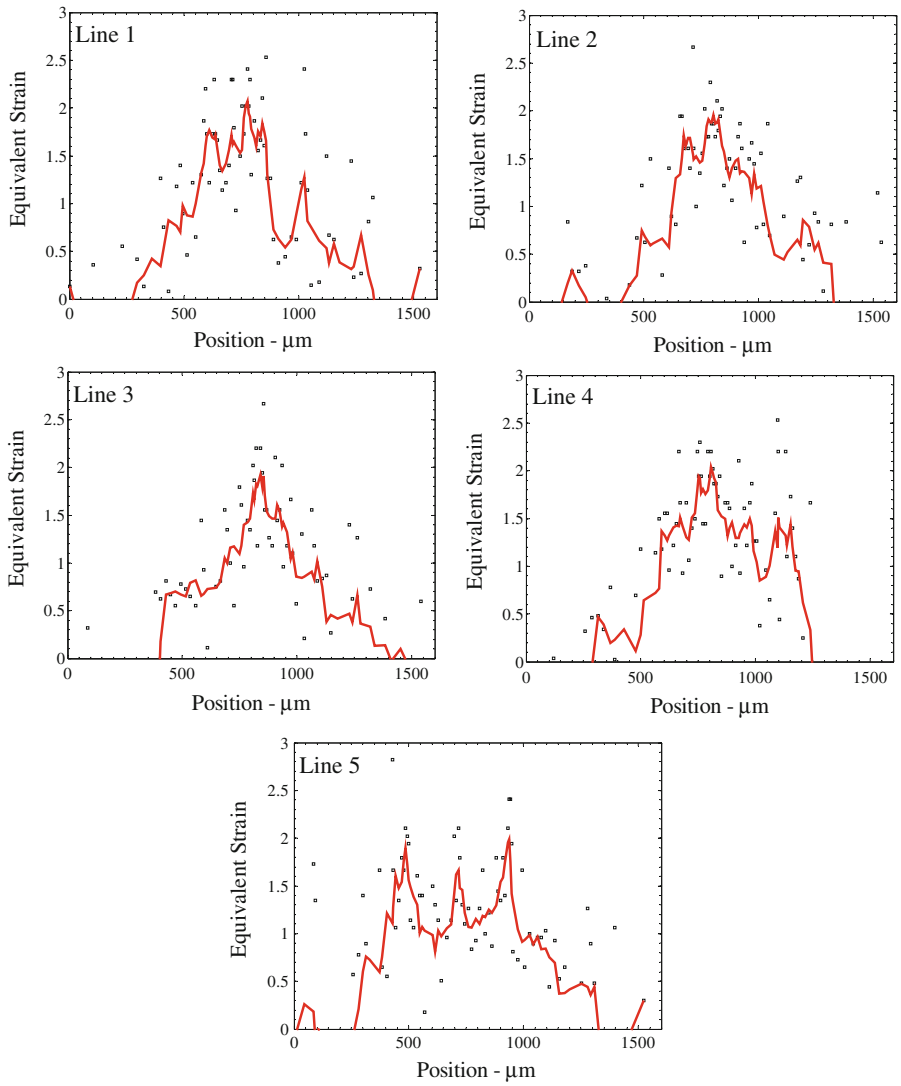

Fig. 11 Variation of the grain-based equivalent strain across Lines 1–5 marked on the Figures 9 and 10. The *symbols* correspond to grain based strain estimates; the *red line* indicates an average over five grains

long, but in the deformed microstructure, the particles are broken into smaller pieces that are 2 µm wide, and between 2 and 4 µm long.

b. A high magnification SEM image of the crack tip region in Specimen S-4 is shown in Fig. 14. While clustering of second phase particles is observed, the SEM images do not indicate the development of cavities near the second phase particles; the equivalent plastic strains in these regions are on the order of 2. There are a few elongated cracks or cavities very close to the crack surface as seen in the figure (at a distance of less than about 10 µm). From comparison with the optical micrographs that reveal the grain boundaries, it appears that these cracks could be along the grain boundaries, but this requires a more refined microscopic examination of the grains.

c. A fractograph of Specimen S-5 is shown in Fig. 15; it is difficult to obtain pristine fracture surfaces since the two mating fracture surfaces rub against each other during continued loading and destroy most of the features on the fracture surface. However, some regions survive without such damage and the images of these regions exhibit elongated dimples on the fracture surface. These are, of course, suggestive of nucleation, growth and coalescence of voids. However, as in the case of the flat-notched tension tests (Ghahremaninezhad and

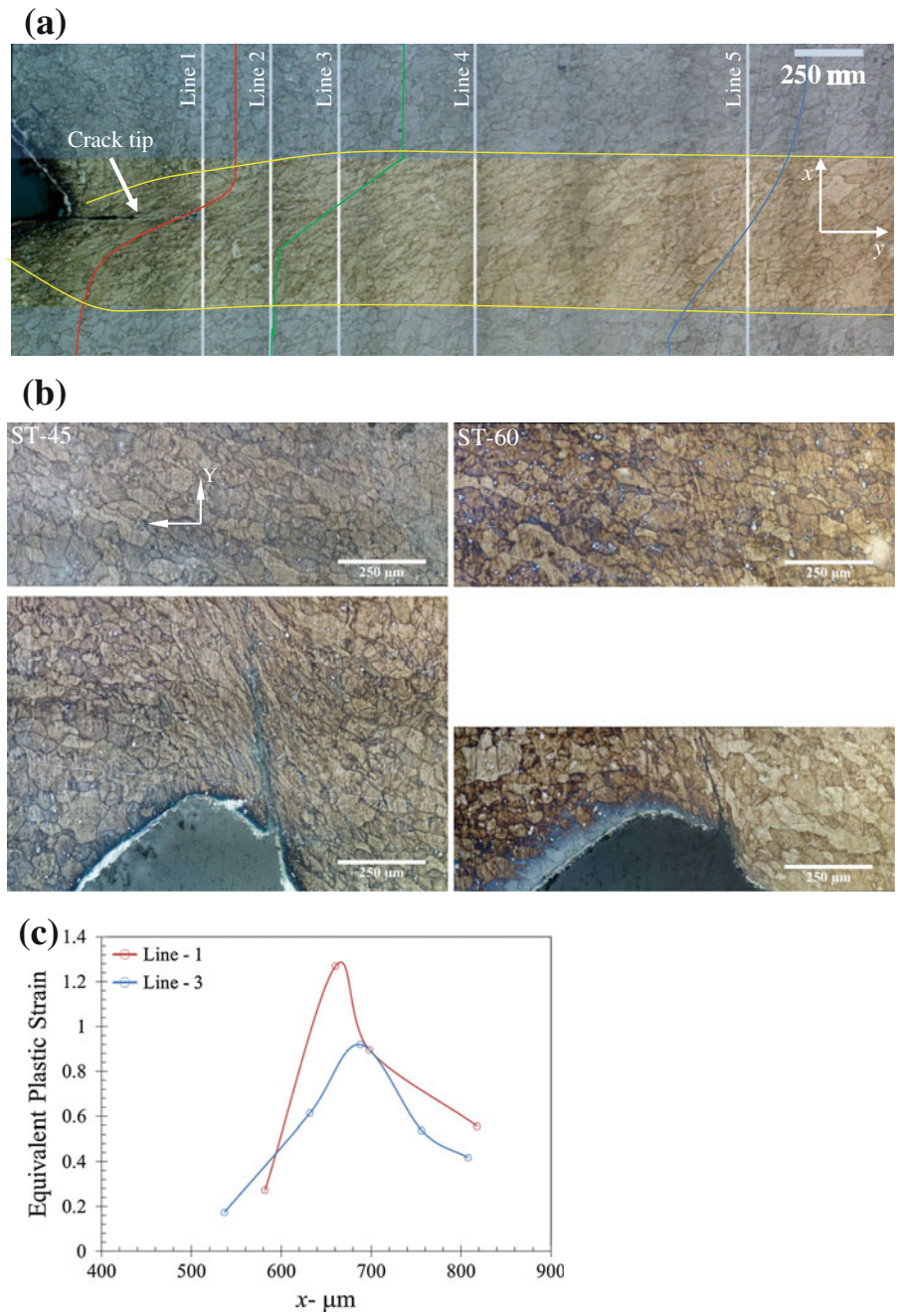

Fig. 12 **a** Micrograph of ST-30. The stage of deformation corresponds to crack initiation marked by the *square* symbol in Fig. 7. **b** Micrographs of the region in the center (*top row*) and near the notch (*bottom row*) of Specimens ST-45 and ST-60. Large grain rotations and deformations are seen in both specimens at the notch where crack extension is observed with those being more pronounced in Specimen ST-45. Grains appear to have experienced small deformation and been aligned with the loading direction in the center of both specimens. **c** Variation of strain across Lines 1 and 3 shown in Fig. 12a

Ravi-Chandar 2012), this failure process occurs in a very narrow localized plane; this can be argued by noting that while numerous dimples are observed on the fracture surface, virtually no cavities are observed below the crack surface in Fig. 14.

d. In the middle regions of the Arcan specimen, the triaxiality is expected to be close to zero. *The observations reported here imply that nucleation of damage does not occur at least until* ≥ 2. This result is in contrast to the cusp-like behavior reported by Beese et al. (2010) and Barsoum and

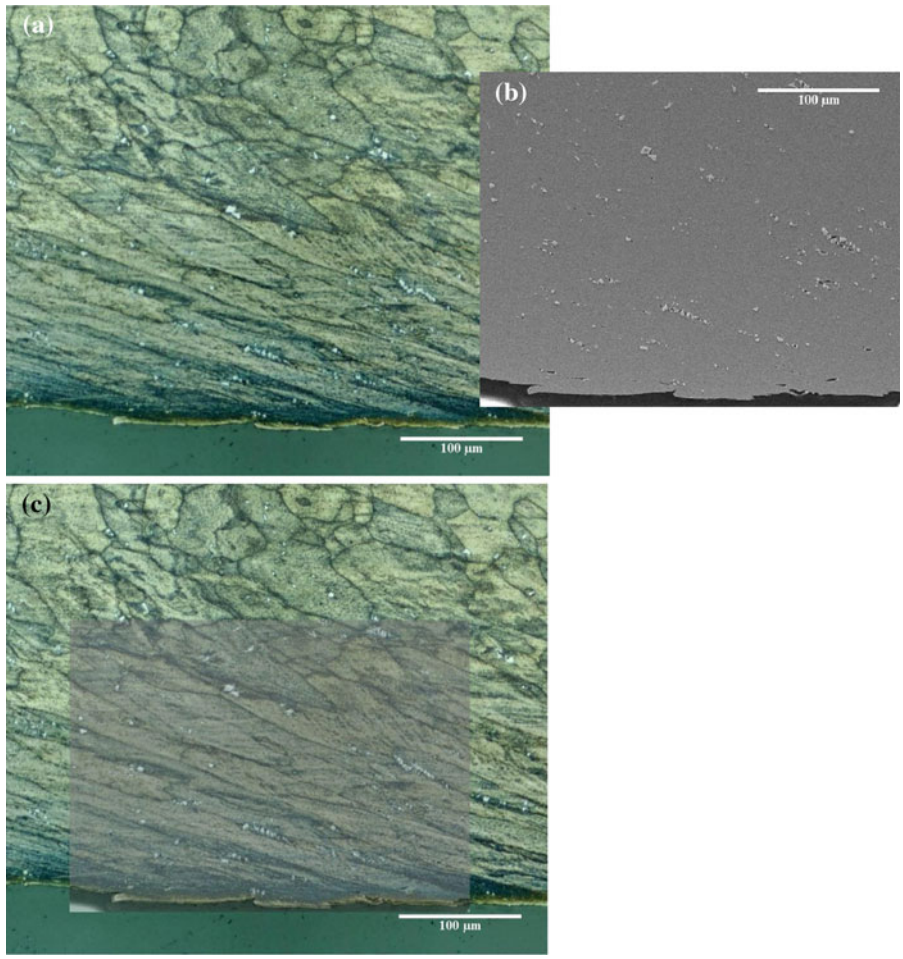

Fig. 13 **a** Optical micrograph and **b** SEM micrograph of the central region of Specimen S-5, and **c** composite overlay of (**b**) onto (**a**) with opacity of 0.6 indicates the location of the second phase particles relative to the grains

Faleskog (2007). Note that the present results are based on local measurements of strain, and microscopic identification of the onset of damage.

In order to examine the microscopic process of deformation and failure under different stress triaxiality, SEM micrographs of Specimen ST-30, ST-45 and ST-60 showing a region below the fracture surface in each specimen are shown in Fig. 16. It is evident form these figures that the grains below the fracture surface appear to be aligned[3] in the direction of the overall loading, and have experienced deformation which seems to decrease as the normal component of the loading increases. Yet, an important observation here is that there are just a few sporadic cavities within 30 μm of the fracture surface, and the region farther away does not appear to contain any cavities.

[3] This alignment could be identified by recognizing that the elongated second phase particles were initially aligned along the vertical direction and have been broken up and rearranged by the deformation.

4 Determination of the strain-to-failure

The grain based strain measurements suggest that damage does not occur until very large strain levels. In order to place these strain measurements in the perspective of the various models of ductile failure such as the Johnson-Cook and the MMC strain-to-failure models, we need to estimate the triaxiality corresponding to the different loading conditions. For the case of the pure shear experiment, the notch tip region should experience, by symmetry, a triaxiality of zero; in practice, small fluctuations could be expected about this value due to small misalignments in mounting, although care was taken in positioning the specimens. Therefore, the pure shear experimental results could be taken as an

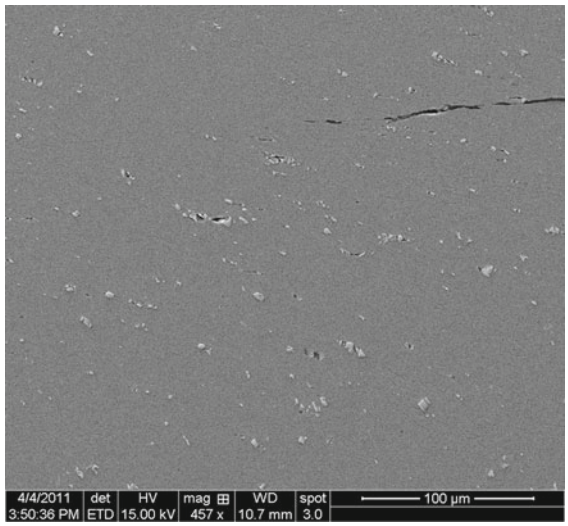

Fig. 14 Very high magnification SEM image of the crack tip region in Specimen S-4. Some of the larger second phase particles may be observed to be broken

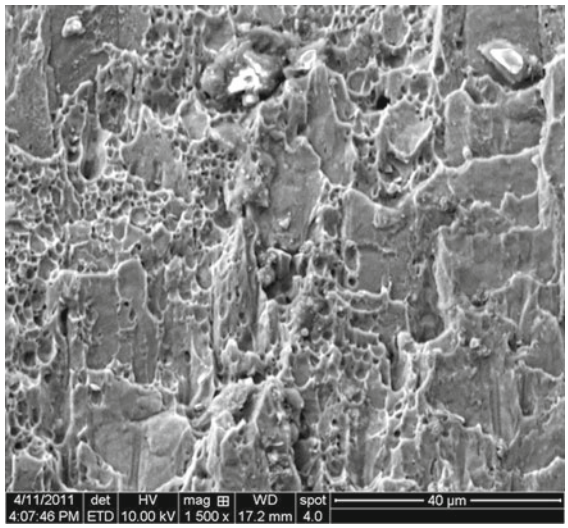

Fig. 15 Fractograph of Specimen S-5. Dimples are observed on the fracture surface indicating void growth and coalescence. Large smooth regions without voids are also observed; it is not clear whether these are feature of the fracture surface due to grain boundary cracking or if they arise from scraping of the opposing fracture surfaces. This requires more sophisticated diagnostic tools

indication that near the notch tip region, the material points exhibit equivalent strains in the range of 2–2.5 and still do not show any signs of failure. We identify this observation on a plot of the variation of the strain-to-failure with triaxiality in Fig. 17 by the blue ellipse; this is meant to imply that we have measured strain levels and triaxialities in this range, but no damage or failure. Therefore, failure will initiate beyond the levels indicated by the ellipse as suggested by the arrow. Additionally, it was shown by Ghahremaninezhad and Ravi-Chandar (2012) that strains of about 1.0 could be measured in the flat notched tension specimens just before the final failure (but without any indication of damage) where the stress triaxiality was estimated to be in the range of 0.8–1. This is shown also in Fig. 17 by another blue ellipse at the corresponding triaxiality range. For contrast, we show the Johnson-Cook failure criterion calibrated by Lesuer et al. (2001) and the Modified Mohr-Coulomb criterion of Beese et al. (2010) for the same type of Al 6061-T6 alloy; it is evident from the present work that material points near the notch tip are able to strain to significantly larger strain levels without damage or failure than would be suggested by the failure criteria that are calibrated from macroscopic strain measurements.

In order to place the observations from the combined shear and tension specimens on the plot of strain-to-failure versus triaxiality, we need to estimate the triaxiality; while a simple estimate of the triaxiality may be obtained as indicated by Mohr and Henn (2007), we need the stress triaxiality on the specimen surface which is where the grain based strains are measured. Therefore, we performed numerical simulations using the finite element software ABAQUS/Explicit 6.9-EF in order to gain an understanding of the stress state in the specimen surface when failure was incipient. The gage section of the Arcan specimen was discretized using 20×200 wedge elements (C3D6) in thickness and width directions, respectively, with particular attention paid to the mesh near the notch tip regions. The elements were gradually coarsened in the areas farther away from the gage section. In order to increase the computational efficiency, variable mass scaling with minimum stable time increment of 10^{-6} s was adopted. The model is subjected to a zero velocity in y-direction on the bottom surface and a velocity ratio of $\sqrt{3}$ in y- and x-directions on the top surface to simulate a specimen loaded at 30° to the y-direction. Both the top and bottom surfaces are constrained against out of plane displacements and rotations. From the large grain rotations and deformations of the grains observed in the experiments, it should be evident that the evolution of anisotropy should be incorporated in the constitutive model, but the calibration of such models to the large deformation response is difficult. In

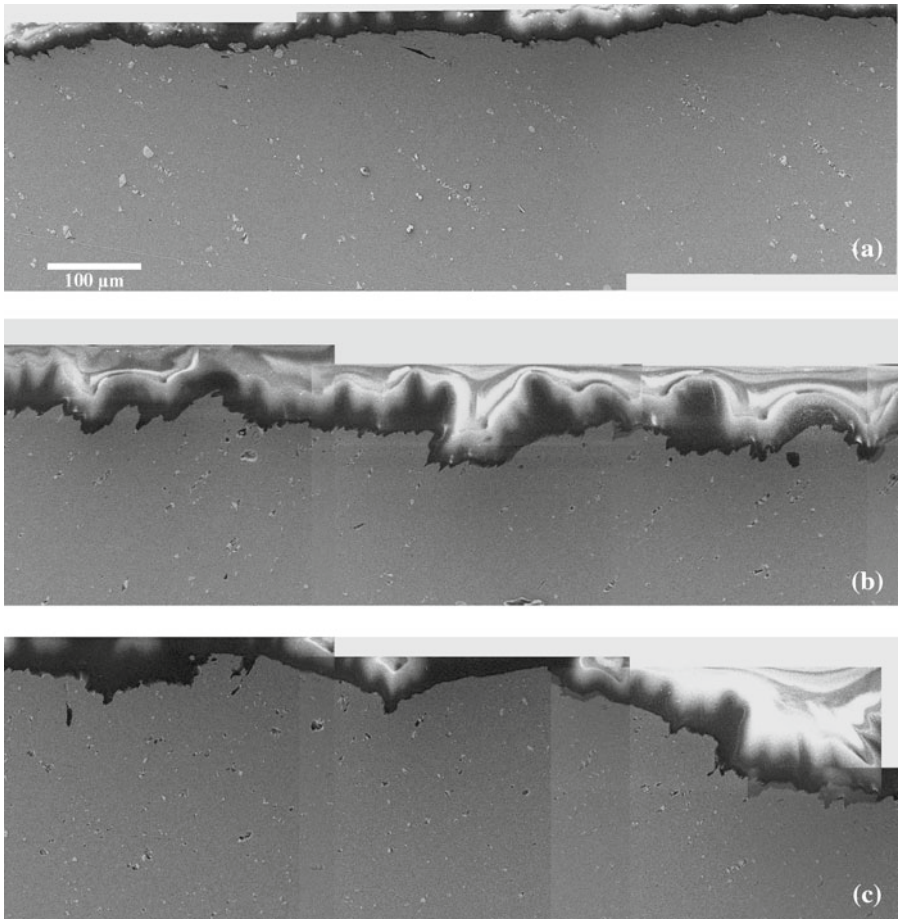

Fig. 16 SEM micrographs of the region below the fracture surface of **a** Specimen ST-30, **b** Specimen ST-45 and **c** Specimen ST-60. With increasing triaxiality, the second phase particles appear to break up more, but not rotate

order to overcome this hurdle, we adopt the Hill anisotropic plasticity model with isotropic hardening rule to model the material behavior; the stress-strain curve and the Lankford parameters for the material given by Ghahremaninezhad and Ravi-Chandar (2012) are used; it is important to note that the material continues to exhibit a modest strain hardening response for very large strain levels. More sophisticated phenomenological anisotropic plasticity models have been proposed which include identification of a large number of parameters (Barlat et al. 2003). In a recent paper, Sreeramulu et al. (2010) used a crystal plasticity model to perform a numerical study of the mode I and II crack tip fields in polycrystalline plastic solids. They concluded that significant texture evolution occurred over a large region particularly under mode II loading and that the predictions of the Hill model differed significantly from the crystal plasticity model predictions. Nevertheless, since the main goal here is to obtain the variation of stress triaxiality in the specimen—rather than a complete prediction of material response—the material model adopted here is deemed appropriate for the numerical simulation.

In order to take into account the effect of small crack growth on the stress triaxiality near the notch tip region, the element deletion feature within ABAQUS/Explicit was activated. The damage initiation criterion for use is obtained using the estimates of strain-to-failure corresponding to pure shear in the present work (nearly zero triaxiality), and the flat notched tension specimen from Ghahremaninezhad and Ravi-Chandar (2012). An exponential variation of strain-to-failure vs. triaxiality is assumed to connect between these two points for numerical simulation. The variation of stress triaxiality in the gage section along y-axis on the *surface* of the 30° specimen is plotted in Fig. 18. It is seen from this plot that after some oscillation near the nucleated crack tip the value of stress triaxiality remains almost

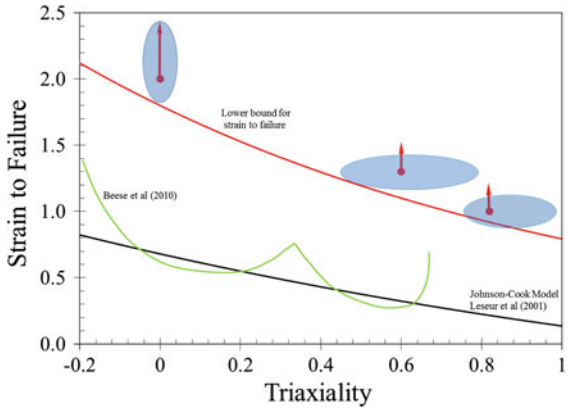

Fig. 17 Variation of strain to failure with triaxiality. The *blue ellipses* indicate the range of strain levels obtained from grain level measurements without damage at the levels of triaxiality indicated. Based on these, a lower bound estimate for the failure strain is suggested by the *red line*

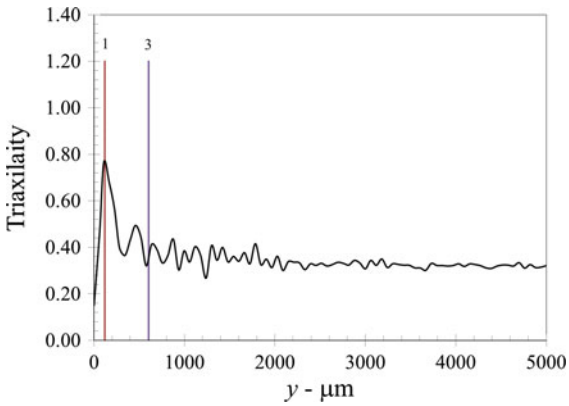

Fig. 18 Variation of the stress triaxiality along the gage section with $y = 0$ coinciding with the notch tip. The location of Lines 1 and 3 marked on Fig. 12a are also indicated and correspond to the *onset* of crack initiation marked by the *square* symbol in Fig. 12

constant over much of the gage section at about 0.4. The oscillation is attributed to the use of the element deletion feature in ABAQUS/Explicit 6.9-EF. The locations of Lines 1 and 3 of Fig. 12a are marked in Fig. 18; it is clear that the triaxiality in the region near the crack tip is in the range of 0.4 – 0.8. The maximum strains measured in the 30° specimen between Lines 1 and 3 in Fig. 12a, as indicated in Fig. 12c are in the range of 1 – 1.3, without showing indications of failure; this is shown in Fig. 17 as a blue ellipse at the corresponding triaxiality range.

Figure 17 represents the *principal result* of this examination into failure of ductile Al 6061-T6 under shear-dominant loading. The three large ellipses *indicate strain levels that could be reached without damage* in the pure shear and the combined shear plus tension tests reported here, and the flat-notched tensions tests reported in Ghahremaninezhad and Ravi-Chandar (2012). Failure occurs when these thresholds are exceeded. Therefore, we draw a bounding line below the ellipses and suggest that this could be used as a lower bound for the actual strain-to-failure, recognizing that this is indeed a conservative estimate. It should be noted from this plot that (i) the lower bound strain-to-failure suggested by grain level measurements is indeed significantly higher in comparison with macroscopic strain measurements and (ii) the strain-to-failure decreases monotonically with stress triaxiality in stark contrast with the results by Bao and Wierzbicki (2004); Beese et al. (2010), and Barsoum and Faleskog (2007) where strain-to-failure increases with stress triaxiality in the range 0–0.3. The lower bound estimate of the strain-to-failure can be fitted with an exponential form $\varepsilon_f = D_2 \exp(D_3 \sigma_m/\sigma_e)$ corresponding to the Johnson-Cook model, where σ_m is the mean stress and σ_e is the effective stress; the parameters of the model are found through a simple fitting procedure: $D_2 = 1.8$ and $D_3 = -0.82$. It should be recognized that this estimate of the strain-to-failure can be used only when the length scales at which such criterion is used are on the order of the grain size.

5 Summary and conclusion

In this article, ductile failure in Al 6061-T6 under shear-dominant loading conditions is investigated. Arcan type specimens under pure shear, and superposed tension and compression were interrupted prior to complete failure, and prepared for metallographical observations. Digital image correlation was used to obtain strain evolution at macro-scale during the loading phase. The grain-based strains were estimated post-test through direct measurements of the change in grain size to characterize the deformation at micro-scale. Scanning electron microscopy was employed to track the evolution of damage in the microstructure. It was observed that cracks initiate at the notches at some point during the deformation; these cracks propagate with further deformation until they reach each other at the center of the specimen resulting in the final separation of the specimen. Strain levels in the range of 1.5 were

measured in the central portion of an interrupted specimen (partially fractured). The two major conclusions are as follows:

1. Quite strikingly, *no damage was observed* in the regions of high strain even while strain levels in the range of 2 were observed near the crack surface and crack tip; a few elongated cracks or cavities were identified very close to the crack surface at a distance of less than about 10 μm. The fracture surfaces exhibit elongated dimples characteristic of void nucleation, growth and coalescence; however, as in the case of the flat-notched tension tests, this failure process occurs in a very narrow localized plane.
2. Comparison with some strain-to-failure models such as the Johnson-Cook model and Modified Mohr Coulomb model shows that the strain values measured at the grain level are significantly larger. The discrepancy between these models and our experimental results is attributed to the possible selection of an inappropriately large gage length over which the strain is measured in conventional tests; in contrast, the present experimental results use a gage-length that is based on the characteristic microstructural length—the grain size. Based on strain measurements at the grain size, we suggest a lower-bound estimate for the strain-to-failure and its dependence on the triaxiality.

Finally, we note that while we have provided a lower bound estimate for the strain at the onset of failure, we have not modeled the failure process.

Acknowledgments This work was performed during the course of an investigation into ductile failure under two related research programs funded by the Office of Naval Research: MURI project N00014-06-1-0505-A00001 and FNC project: N00014-08-1-0189. This support is gratefully acknowledged.

References

Aoki S, Kishimoto K, Yoshida T, Sakata M, Richard HA (1990) Elastic-plastic fracture behavior of an aluminum alloy under mixed mode loading. J Phys Mech Solids 38:195–213

Bao Y, Wierzbicki T (2004) On fracture locus in the equivalent strain and stress triaxiality space. Int J Mech Sci 46:81–98

Barlat F, Brem JC, Yoon JW, Chung K, Dick RE, Lege DJ, Pourboghrat F, Choi S-H, Chu E (2003) Plane stress function for aluminum alloy sheets—Part I: theory. Int J Plast 19:1297–1319

Barsoum I, Faleskog J (2007) Rupture in combined tension and shear: experiments. Int J Solids Struct 44:1768–1786

Beese AM, Luo M, Li Y, Bai Y, Wierzbicki T (2010) Partially coupled anisotropic fracture model for aluminum sheets. Eng Fract Mech 77:1128–1152

Dunand M, Mohr D (2011) Optimized butterfly specimen for the fracture testing of sheet materials under combined normal and shear loading. Eng Fract Mech 78:2919–2934

Ghahremaninezhad A, Ravi-Chandar K (2011) Ductile failure in polycrystalline OFHC copper. Int J Solids Struct 48:3299–3311

Ghahremaninezhad A, Ravi-Chandar K (2012) Ductile failure behavior of polycrystalline Al 6061-T6. Int J Fract 174:177–202

Ghosal AK, Narasimhan R (1994) A finite element analysis of mixed-mode fracture initiation by ductile failure mechanisms. J Phys Mech Solids 42:953–978

Ghosal AK, Narasimhan R (1996) Numerical simulations of hole growth and ductile fracture initiation under mixed-mode loading. Int J Fract 77:281–304

Ghosal AK, Narasimhan R (1997) A finite element study of the effect of void initiation and growth on mixed-mode ductile fracture. Mech Mater 25:113–127

Haltom SS, Kyriakides S, Ravi-Chandar K (2012) Ductile failure under combined shear and tension. Int J Solids Struct (to appear)

Hancock JW, Mackenzie AC (1976) On the mechanisms of ductile failure in high-strength steels subjected to multi-axial stress-states. J Mech Phys Solids 24:147–169

Hung SC, Liechti KM (1997) An evaluation of the Arcan specimen for determining the shear moduli of fiber reinforced composites. Exp Mech 37:460–468

Hung S-C, Liechti KM (1999) Finite element analysis of the Arcan specimen for fiber reinforced composites under pure shear and biaxial loading. J Compos Mater 33:1288–1317

Johnson GR, Cook WH (1985) Fracture characteristics of three metals subject to various strains, strain rates, temperatures and pressures. Eng Fract Mech 21:31–48

Kamat SV, Hirth JP (1996) Mixed Mode I/II fracture toughness of 2034 aluminum alloys. Acta Mater 44:201–208

Lesuer DR, Kay GJ, LeBlanc MM (2001) Modeling large strain, high-rate deformation in metals. UCRL-JC-134118, Lawrence Livermore National Laboratory

Lindholm US, Nagy A, Johnson GR, Hoegfeldt JM (1980) Large strain, high strain rate testing of copper. J Mater Eng Technol 102:376–381

Mohr D, Henn S (2007) Calibration of stress-triaxiality dependent crack formation criteria: a new hybrid experimental-numerical method. Exp Mech 47:805–820

Nahshon K, Hutchinson JW (2008) Modification of the Gurson model for shear. Eur J Mech A/Solids 27A:1–17

Puttick KE (1960) Shear component of ductile failure. Philos Mag 5:759–762

Rogers HC (1960) The tensile fracture of ductile metals. Trans Metall Soc AIME 218:498–506

Roy Y, Narasimhan R, Arora PR (1999) An experimental investigation of constraint effects on mixed mode fracture initiation in a ductile aluminum alloy. Acta Mater 47:1587–1596

Sreeramulu K, Sharma P, Narasimhan R, Mishra R (2010) Numerical simulations of crack tip fields in polycrystalline plastic solids. Eng Fract Mech 77:1253–1274